In conclusion, we could better visualize the LSA with FSBB acquisition than with TOF-MRA, both quantitatively and qualitatively. The FSBB scan is considered a promising method, but it remains to be evaluated in clinical cases.

REFERENCES

1. Marinkovic S, Gibo H, Milisavljevic M, Cetkovic M. Anatomic and clinical correlations of the lenticulostriate arteries. Clin Anat 2001; 14:190–195.
2. Marinkovic SV, Kovacevic MS, Marinkovic JM. Perforating branches of the middle cerebral artery. Microsurgical anatomy of their extracerebral segments. J Neurosurg 1985;63:266–271.
3. Feekes JA, Hsu SW, Chaloupka JC, Cassell MD. Tertiary microvascular territories define lacunar infarcts in the basal ganglia. Ann Neurol 2005;58:18–30.
4. Feekes JA, Cassell MD. The vascular supply of the functional compartments of the human striatum. Brain 2006;129:2189–2201.
5. Wardlaw JM, Dennis MS, Warlow CP, Sandercock PA. Imaging appearance of the symptomatic perforating artery in patients with lacunar infarction: occlusion or other vascular pathology? Ann Neurol 2001;50:208–215.
6. Wang X, Lam WW, Fan YH, Graham CA, Rainer TH, Wong KS. Topographic patterns of small subcortical infarcts associated with MCA stenosis: a diffusion-weighted MRI study. J Neuroimaging 2006;16:266–271.
7. Haacke EM, Xu Y, Cheng YC, Reichenbach JR. Susceptibility weighted imaging (SWI). Magn Reson Med 2004;52:612–618.
8. Reichenbach JR, Barth M, Haacke EM, Klarhofer M, Kaiser WA, Moser E. High-resolution MR venography at 3.0 Tesla. J Comput Assist Tomogr 2000;24:949–957.
9. Wang Y, Yu Y, Li D, et al. Artery and vein separation using susceptibility-dependent phase in contrast-enhanced MRA. J Magn Reson Imaging 2000;12:661–670.
10. Le Bihan D, Breton E, Lallemand D, Aubin ML, Vignaud J, Laval-Jeantet M. Separation of diffusion and perfusion in intravoxel incoherent motion MR imaging. Radiology 1988;168:497–505.
11. Kimura T, Ikedo M, Furudate N, Takemoto S. Flow-sensitive susceptibility-weighted imaging. In: Proc Joint Annual Meeting ISMRM-ESMRMB, Berlin; May 19–25, 2007:3015.
12. Tsuchiya K, Tateishi H, Yoshida M, et al. Flow-sensitive susceptibility-weighted imaging of the brain: initial experience in ischemic lesions. In: Proc Joint Annual Meeting ISMRM-ESMRMB, Berlin; May 19–25, 2007:3016.
13. Fushimi Y, Miki Y, Kikuta K, et al. Comparison of 3.0- and 1.5-T three-dimensional time-of-flight MR angiography in moyamoya disease: preliminary experience. Radiology 2006;239:232–237.
14. Nakano S, Iseda T, Kawano H, Yoneyama T, Ikeda T, Wakisaka S. Correlation of early CT signs in the deep middle cerebral artery territories with angiographically confirmed site of arterial occlusion. AJNR Am J Neuroradiol 2001;22:654–659.
15. Bradley WG Jr, Waluch V. Blood flow: magnetic resonance imaging. Radiology 1985;154:443–450.
16. Gillams AR, McMahon L, Weinberg G, Carter AP. MRA of the intracranial circulation in asymptomatic patients with sickle cell disease. Pediatr Radiol 1998;28:283–287.
17. Sasaki T, Kodama N, Matsumoto M, et al. Blood flow disturbance in perforating arteries attributable to aneurysm surgery. J Neurosurg 2007;107:60–67.
18. Park DH, Kang SH, Lee JB, et al. Angiographic features, surgical management and outcomes of proximal middle cerebral artery aneurysms. Clin Neurol Neurosurg 2008;110:544–551.
19. Marinkovic S, Milisavljevic M, Marinkovic Z. Anastomoses among the perforating arteries of the brain. Microanatomy and clinical significance. Neurologija 1990;39:107–114.
20. Ghika J, Bogousslavsky J, Regli F. Infarcts in the territory of lenticulostriate branches from the middle cerebral artery. Etiological factors and clinical features in 65 cases. Schweiz Arch Neurol Psychiatr 1991;142:5–18.
21. Ahn JY, Cho JH, Lee JW. Distal lenticulostriate artery aneurysm in deep intracerebral haemorrhage. J Neurol Neurosurg Psychiatry 2007;78:1401–1403.

European Journal of Radiology 73 (2010) 114–118

Contents lists available at ScienceDirect

European Journal of Radiology

journal homepage: www.elsevier.com/locate/ejrad

High spatial resolution 3D MR cholangiography with high sampling efficiency technique (SPACE): Comparison of 3 T vs. 1.5 T

Shigeki Arizono*, Hiroyoshi Isoda, Yoji S. Maetani, Yuusuke Hirokawa, Kotaro Shimada, Yuji Nakamoto, Toshiya Shibata, Kaori Togashi

Department of Diagnostic Imaging and Nuclear Medicine, Kyoto University Graduate School of Medicine, 54 Shogoin Kawahara-cho, Sakyo-ku, Kyoto 606-8507, Japan

ARTICLE INFO

Article history:
Received 4 June 2008
Received in revised form 5 August 2008
Accepted 6 August 2008

Keywords:
High field
3 T
MR cholangiography
SPACE
High resolution
3D

ABSTRACT

Purpose: The aim of this study was to evaluate image quality of 3D MR cholangiography (MRC) using high sampling efficiency technique (SPACE) at 3 T compared with 1.5 T.
Methods and materials: An IRB approved prospective study was performed with 17 healthy volunteers using both 3 and 1.5 T MR scanners. MRC images were obtained with free-breathing navigator-triggered 3D T2-weighted turbo spin-echo sequence with SPACE (TR, >2700 ms; TE, 780 ms at 3 T and 801 ms at 1.5 T; echo-train length, 121; voxel size, 1.1 mm × 1.0 mm × 0.84 mm). The common bile duct (CBD) to liver contrast-to-noise ratios (CNRs) were compared between 3 and 1.5 T. A five-point scale was used to compare overall image quality and visualization of the third branches of bile duct (B2, B6, and B8). The depiction of cystic duct insertion and the highest order of bile duct visible were also compared. The results were compared using the Wilcoxon signed-ranks test.
Results: CNR between the CBD and liver was significantly higher at 3 T than 1.5 T ($p = 0.0006$). MRC at 3 T showed a significantly higher overall image quality ($p = 0.0215$) and clearer visualization of B2 ($p = 0.0183$) and B6 ($p = 0.0106$) than at 1.5 T. In all analyses of duct visibility, 3 T showed higher scores than 1.5 T.
Conclusion: 3 T MRC using SPACE offered better image quality than 1.5 T. SPACE technique facilitated high-resolution 3D MRC with excellent image quality at 3 T.

1. Introduction

Magnetic resonance cholangiography (MRC) has been accepted as a powerful imaging modality for the assessment of biliary disorders [1–5]. However, conventional MRC using the heavily T2-weighted turbo spin-echo (TSE) technique with two-dimensional (2D) thick-slab or 2D multislice at 1.5 T MR units is insufficient to evaluate the intrahepatic bile duct (IHBD), particularly if the biliary system is not dilated, because of limited spatial resolution and the signal-to-noise ratio (SNR) [6–8]. Therefore, the utility of MRC is restricted when detailed anatomic information of the non-dilated IHBD is needed, for example, for the preoperative assessment of living-related liver transplant donors [6,9,10].

Recently, 3 T whole-body MR scanners have been introduced and become available for upper abdominal imaging [11,12]. They can facilitate high-quality MRC, reflecting the abundant SNR. Some investigators have reported that MRC at 3 T has the potential to improve the visualization of anatomic details compared to 1.5 T [7,13,14]. However, specific absorption ratio (SAR) deposition is sometimes problematic at 3 T, which might force us to reluctantly change protocols, especially in three-dimensional (3D) TSE sequence.

To avoid the SAR problem, a new technique of Sampling Perfection with Application optimized Contrasts using different flip angle Evolutions, called SPACE, has been proposed. This sequence is a variant of 3D TSE, and uses a variable flip angle less than 180°, which allows a larger number of refocusing pulses to be used per repetition time while good T2-weighted contrast and low SAR are maintained without reducing a better SNR at 3 T [15–17]. In our previous study, we proved that high spatial resolution 3D MRC with SPACE at 3 T produces higher image quality of the biliary tract compared to 3D MRC with the usual constant flip angle TSE sequence, and has the ability to depict the non-dilated IHBD [18]. Haystead et al. also recently reported the superiority of the SPACE technique over conventional constant flip angle TSE sequence in 3D MRC at 3 T [17]. To the best of our knowledge, however, no report has made a comparison of 3D MRC with SPACE between 3 and 1.5 T. Thus, the aim of this study was to evaluate the image quality of 3D MRC with

* Corresponding author. Tel.: +81 75 751 3419; fax: +81 75 771 9709.
E-mail addresses: arizono@kuhp.kyoto-u.ac.jp (S. Arizono), sayuki@kuhp.kyoto-u.ac.jp (H. Isoda), mbo@kuhp.kyoto-u.ac.jp (Y.S. Maetani), yuusuke@kuhp.kyoto-u.ac.jp (Y. Hirokawa), kotaro@kuhp.kyoto-u.ac.jp (K. Shimada), ynakamo1@kuhp.kyoto-u.ac.jp (Y. Nakamoto), ksj@kuhp.kyoto-u.ac.jp (T. Shibata), ktogashi@kuhp.kyoto-u.ac.jp (K. Togashi).

0720-048X/$ – see front matter © 2008 Elsevier Ireland Ltd. All rights reserved.
doi:10.1016/j.ejrad.2008.08.003

Table 1
MR cholangiography sequence parameters

	3 T	1.5 T
TR (ms)	2987–7699[a]	2727–8109[a]
TE (ms)	780	801
Flip angle (°)	[b]	[b]
Echo-train length	121	121
Parallel acquisition technique factor	3	3
No. of signals acquired	2	2
Field of view (mm)	400	400
Inplane resolution (mm)	1.1 × 1.0	1.1 × 1.0
Slice thickness (mm)	0.84	0.84
Slice number	88	88
Acquisition time (min)	3–6[c]	3–6[c]

[a] TR differs among subjects according to respiratory cycle.
[b] Flip angles of the refocusing pulses are variable. The flip angle evolution in SPACE is calculated in order to achieve a high and nearly constant signal of tissues during large part of signal acquisition.
[c] Acquisition time differs among subjects according to respiratory cycle.

SPACE at 3 T compared to 3D MRC with SPACE at 1.5 T, and to assess the advantage of the SPACE technique for achieving high-resolution 3D MRC at 3 T.

2. Materials and methods

2.1. Study design

In a prospective study, 17 healthy volunteers (11 men, 6 women; age range, 26–57 years; mean age, 37 years) were assigned to undergo MRC on both 3 and 1.5 T MR scanners. All volunteers fasted for at least 5 h before the scan, and were examined in random order on both units within a time interval of 2 h. They did not receive any oral contrast agents to suppress bowel signals.

The local institutional review board first approved all MR imaging examinations, and all volunteers gave their written informed consent before the study protocol commenced.

2.2. MRC protocols

MRC imaging was performed at two different commercially available MR systems in the Magnetom series of Siemens (Erlangen, Germany): Magnetom Trio (3 T) and Magnetom Symphony (1.5 T). At 3 T, an eight-channel transmit–receive phased-array coil was used to obtain the images. At 1.5 T, a six-channel transmit–receive phased-array body coil was used. At 3 T, the images were obtained by placing a dielectric pad with US gel doped with Gd-DTPA (RF cushion; Siemens) in front of the body to prevent B1 inhomegeneity caused by the dielectric effect. Prior to MRC, we performed T1-weighted fast low-angle shot sequences and breath-hold T2-weighted TSE sequences to localize the biliary tree. Free-breathing navigator-triggered 3D T2-weighted TSE imaging with SPACE was used to obtain MRC images at each scanner. The prospective acquisition correction (PACE) technique was used to correct respiratory motion. Phase encoding was performed in the left–right direction. The iPAT reconstruction was performed in one direction in the plane of the image slice in the phase-encoding direction. The GRAPPA algorithm was used for the iPAT, and the coil sensitivity information was based on 24 k-space lines. No half-Fourier or filtering techniques were applied. The imaging protocols at 3 and 1.5 T are shown in Table 1. We performed MRC imaging with the same parameters as much as possible, but some different parameters were adopted due to restriction of the device and the sequences provided by the vendor. All MRC images were obtained in the coronal oblique plane at angles parallel to the hepatic hilum.

2.3. Quantitative image analysis

All quantitative and qualitative assessments of the image quality were performed at a commercially available workstation (Ziostation, Ziosoft, Tokyo, Japan). To quantify the image quality of MRC, the common bile duct (CBD) to liver contrast-to-noise ratio (CNR) was measured. One experienced radiologist (10-year experience) conducted operator-defined region-of-interest (ROI) measurements. The signal intensity (SI) of the CBD was measured for each MRC sequence by defining ROIs. ROIs for the SI of the CBD were at least 5 mm^2 and were chosen in homogeneous, artifact-free areas of the middle CBD. To measure SI and the standard deviation (S.D.) of the liver, a single ROI drawn as large as possible was located in a homogenous portion of the liver and set in an area devoid of vessels and prominent artifacts. Because of the inherent inhomogeneity of iPAT images, we could not directly measure the noise. We calculated the S.D. of the liver as the noise ($S.D._{noise}$) instead.

The CBD to the liver CNR was calculated using the following formula: $CNR = (SI_{CBD} - SI_{liver})/S.D._{noise}$.

2.4. Qualitative image analysis

All MRC images were interpreted independently by two experienced radiologists. One operator had 6 years of experience at the beginning of this study, and the other had 17 year's experience. The radiologists were blinded to imaging parameters. Differences were resolved by consensus. If consensus was not achieved, a third reader (14-year experience) determined the score. Maximum intensity projections (MIPs) were generated from each multislice data set on the workstation, and both the source and MIP images from each sequence were used for data analysis.

Visualization of the third branches of the IHBD (B2, B6, and B8) were graded with the use of a five-point scale (5 = excellent, if the duct (third branch) and its branches (fourth branches) could be clearly seen; 4 = good, if the duct could be seen clearly but its branches were moderately visible; 3 = average, if the duct could be seen with moderate visibility but its branches were observable with only limited visibility; 2 = fair, if the duct was visible but the image of the duct was blurred and its branches could not be seen; and 1 = poor, if the duct could not be seen). We chose B2, B6, and B8 for the grading of IHBD imaging because their identification in the biliary tree was relatively easy (Fig. 1a). The depiction of cystic duct insertion was also graded with the use of a three-point scale (3 = clearly depicted; 2 = seen with moderate clarity; 1 = not visible). The overall image quality was assessed on a five-point scale for delineation of the entire biliary system and the presence of artifacts, noise, or both (5 = excellent; 4 = good; 3 = average; 2 = fair; 1 = poor). The highest order of IHBD visible was also recorded.

2.5. Statistics

Statistical analyses were performed using a commercially available software package (Statview, Version 5.0.1; SAS Institute, Cary, NC, USA). The quantitative and qualitative results were compared using the Wilcoxon signed-ranks test. A p-value of less than 0.05 was taken to indicate a significant difference.

3. Results

MRC imaging was performed safely in all subjects without any complications. No volunteers reported thermal sensations during sequences operating near the maximal SAR. Quantitative and qualitative assessments were performed in all 17 volunteers. The results

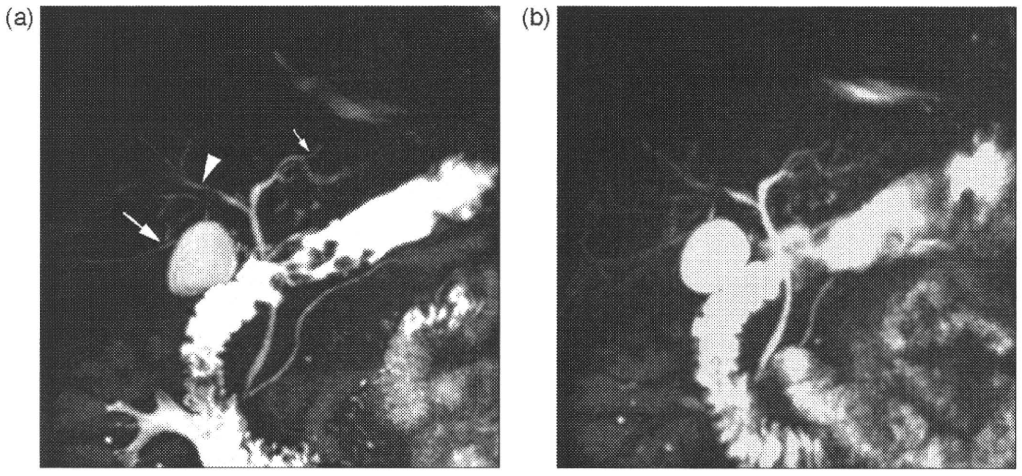

Fig. 1. Comparison of MIP reconstructions of MRC images obtained at 3 T (a) and 1.5 T (b). Third branches of intrahepatic bile ducts are described in (a); B2 (small arrow), B6 (large arrow) and B8 (arrowhead). Visibility of intrahepatic bile ducts was more pronounced on 3 T image.

Table 2
Results of qualitative and quantitative analyses of MRC images obtained at 3 and 1.5 T

	3 T	1.5 T	*p*-Value
CNR between CBD and liver	115 ± 58	75 ± 38	0.0006
B2	3.9 ± 1.3	3.1 ± 1.3	0.0183
B6	3.5 ± 1.4	2.6 ± 1.4	0.0106
B8	4.4 ± 0.9	3.9 ± 1.4	0.1193
Cystic duct insertion	2.6 ± 0.7	2.2 ± 0.8	0.0532
Highest order of IHBD visible	4.2 ± 1.0	3.5 ± 0.9	0.0119
Overall image quality	4.0 ± 1.2	3.1 ± 1.1	0.0215

are summarized in Table 2. Figs. 1 and 2 show examples of MRC images.

3.1. Quantitative image analysis

The CNR between the CBD and liver was 53% higher at 3 T than that at 1.5 T, showing a significant difference.

3.2. Qualitative image analysis

3.2.1. Duct visibility

MRC images obtained at 3 T showed a significantly clearer visualization of B2 and B6 than at 1.5 T. Visualization of B8 showed no significant difference, though the score was higher at 3 T than at 1.5 T. The average of the highest order of IHBD visible on images at 3 T was 4.2 (±1.0); fourth or more peripheral branches of the IHBD were detectable in 13 of 17 volunteers (76%). The result with 1.5 T was 3.5 (±0.9), being significantly inferior to 3 T. In all analyses of duct visibility, MRC images at 3 T showed higher scores than at 1.5 T.

3.2.2. Overall image quality

MRC images obtained at 3 T showed a significantly higher overall image quality than at 1.5 T. Respiratory misregistration was seen in four volunteers; one volunteer in both 3 and 1.5 T images, one in only 3 T images, and two in only 1.5 T images. There were no ghosting or susceptibility artifacts which affected image interpretation on both 3 and 1.5 T images.

4. Discussion

In the present study, we have shown an improvement in image quality on SPACE-using MRC at 3 T compared to 1.5 T. There was also an improvement in the CNR between the CBD and liver. These results are consistent with previous comparison studies of 3D MRC between 3 and 1.5 T. In the study of Merkle et al., involving respiratory-triggered 3D MRC imaging in 15 volunteers, MRC at 3 T offered an improved CNR and a higher level of confidence for

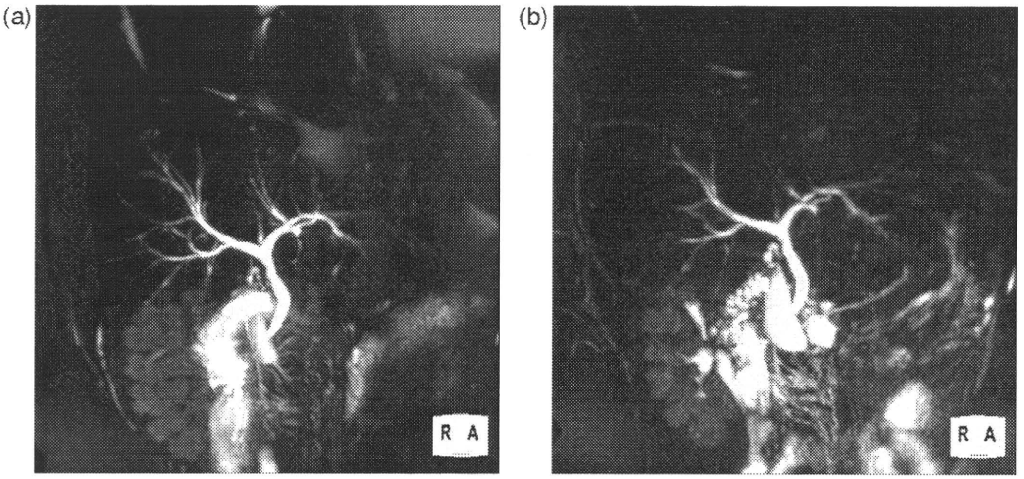

Fig. 2. Other examples of MIP reconstructed MRC images obtained at 3 T (a) and 1.5 T (b). Peripheral intrahepatic bile ducts were excellently depicted on 3 T image.

depicting IHBD variants [7]. Isoda et al. examined 14 volunteers using MRC imaging with respiratory-triggered 3D TSE sequences, and showed that MRC imaging at 3 T provides a significant improvement in duct visibility [14]. In addition to these previous studies, our results suggest the superiority of 3 T MRC over 1.5 T also with the SPACE-using 3D TSE sequence. In contrast, according to Schindera et al., who evaluated two different groups of subject each contained 50 patients at 3 and 1.5 T using MRC with respiratory-triggered 3D TSE, qualitative image analyses did not reveal any significant preference for either field strength [19]. However, 1.5 T sequences may have been closer to the optimum, whereas 3 T sequences were relatively immature, as they discussed in their report.

The present study also revealed that the visibility of the IHBD was markedly enhanced at 3 T. Visualizations of B2 and B6 were significantly better at 3 T compared to 1.5 T, while B8 showed no significant difference. It is possible to assume that abundant SNR at 3 T serves to clearly delineate ducts with a small caliber; generally, B2 and B6 have a smaller caliber compared to B8. At 1.5 T, it is difficult to ensure a sufficient CNR between a small amount of bile fluid and the liver, especially under high-resolution conditions, as in our study. In contrast, the larger caliber of B8 might push up the average scores on both 3 and 1.5 T, which we surmise made difficult to reveal statistically significant difference; indeed the average scores of B8 were higher than B2 and B6 at both 3 and 1.5 T. Because the scores of B8 were also higher at 3 T than at 1.5 T to some extent, further MRC studies involving larger groups could indicate the significant superiority of 3 T over 1.5 T in the visibility of B8.

The improvement in the visibility of the small caliber IHBD was, we assume, achieved by a favorable balance between a high spatial resolution and high SNR. Generally, in upper abdominal imaging at 3 T, the increased SAR is problematic, especially in TSE sequences with long echo trains, because of the high RF power deposition caused by multiple refocusing pulses; this is one of the drawbacks of 3 T. To avoid this, protocol adjustments are often needed, such as decreases in the spatial resolution, number of slices, or the flip angle. These adjustments are undesirable because they reduce resolution and anatomic coverage, alter the contrast, or reduce the signal gain [12,20]. SPACE can overcome these problems and ensure high-resolution images without a decrease in the SNR. In the imaging sequences of the present study, the adopted resolution involved a 1.1 mm × 1.0 mm × 0.84 mm voxel size with 88 slices. This is a higher resolution and larger anatomic coverage than in previous studies of 3D MRC with conventional constant flip angle TSE sequences at 3 T. In these studies, the adopted parameters were: voxel size, 1.35 mm × 1.17 mm × 1 mm; 60 slices [7]: voxel size (before zero-fill interpolation processing), 1.06 mm × 1.06 mm × 1.2 mm; 48 slices [14]: voxel size, 1.25 mm × 1.17 mm × 1 mm; 60 slices [19]: and voxel size (before interpolation processing), 1.25 × 1.17 × 2.0 mm; 72 slices with an interpolated section of 1 mm [17]. These are, respectively, 71, 46, 58, and 217% larger in voxel size, and 19, 22, 19, and 3% smaller in coverage volume compared to our study. In addition, Isoda et al. decreased the flip angle of refocusing pulses to 150° from the ideal flip angle of 180° in order to remain within the accepted SAR range [14], although this might reduce image quality due to a decreased signal gain and change in contrast [16]. Also, in the study of SPACE-using MRC by Haystead et al., adopted parameters were: voxel size (before interpolation processing), 1.25 mm × 1.17 mm × 1.3 mm; 72 slices with an interpolated section of 1 mm [17]. This is 106% larger in voxel size and 3% smaller in coverage volume compared to our study, though smaller in voxel size compared to their constant flip angle sequence. In contrast to these previous studies, we realized high-resolution MRC with excellent image quality using the SPACE technique. The use of the SPACE sequence, which gathers high signal intensities only for the echoes used to acquire the low phase-encoding steps, allows a significant reduction in the SAR, while maintaining the SNR [15,16]. As discussed in our previous work, the SPACE technique should be employed for 3D MRC to make use of the advantage of 3 T, especially when a high spatial resolution and high volume coverage are adopted [18].

On the other hand, there was no significant difference in the visibility of cystic duct insertion between 3 and 1.5 T, although the score was higher with 3 T. This result is consistent with previous studies in which 3D MRC at 3 T provided a slightly better visibility of the cystic duct or cystic duct insertion compared to 1.5 T [7,14]. We speculate that the artifact of gas and/or peristalsis from the duodenum occasionally reduces image quality at the site of cystic duct insertion. Susceptibility artifacts are said to increase at a higher magnetic strength, which might be another drawback of 3 T on MRC imaging [11,12]. However, this is not a major hurdle in applying the 3 T MR system to MRC imaging, because the visibility of the cystic duct was slightly better with 3 T compared to 1.5 T in the studies mentioned above.

The ability to depict non-dilated IHBD may have many clinical applications, including the diagnosis of small hepatolithiasis, primary sclerosing cholangitis, or the preoperative assessment of the biliary system in living-related liver donors. Some authors reported that MRC obtained with conventional 2D methods at 1.5 T has the capability to assess non-dilated biliary anatomy in potential donors but is insufficient in terms of accuracy [6,9,10]. Also, other reports have indicated that iodipamide meglumine-enhanced multidetector row CT (MDCT) cholangiography is superior to MRC (including conventional 2D T2-weighted MRC and mangafodipir trisodium-enhanced excretory MRC) for the preoperative assessment of the biliary tract [21,22], although adverse reactions to CT biliary contrast agents are reportedly observed in 1–3% of subjects [21,23]. On 3D MRC with SPACE at 3 T in our study, the mean score of the third branches of the IHBD were 3.9, and the fourth or more peripheral branches of the IHBD were detectable in 13 of 17 volunteers. Schroeder et al. reported that the third or fourth branches of the IHBD were frequently visualized clearly on MDCT cholangiography [22,23], and our result is comparable to this. 3D MRC with the SPACE technique at 3 T can generate sufficient information on the anatomy of the non-dilated IHBD during the preoperative assessment of potential donors, without the risk of reactions to contrast agents or ionizing radiation exposure.

There were certain limitations in our study. First, only a small number of subjects were assessed to evaluate MRC imaging. Our results should be validated through further studies. Secondly, all MRC images in our study were obtained under free-breathing using the respiratory triggering technique (PACE). A few subjects showed respiratory misregistration even with the PACE technique. Therefore, it might be necessary in clinical examinations to conduct breath-hold MRC (breath-hold thick-slab 2D TSE and/or breath-hold multislice HASTE) in combination with free-breathing navigator-triggered MRC. Thirdly, our study population was healthy, so we do not have data on biliary disorders. Therefore, the clinical utility of 3D MRC with SPACE at 3 T in evaluating pathological states needs to be examined in a patient-based study. Fourthly, phased-array coils used were eight-channel at 3 T and six-channel at 1.5 T. Because phased-array coils with more elements may by themselves increase the SNR compared to coils with less elements, this difference might exaggerate the advantage of 3 T.

5. Conclusions

3 T MRC using SPACE offered better image quality compared to 1.5 T MRC with SPACE, especially in the visualization of the

IHBD. The SPACE technique facilitated high-resolution 3D MRC with excellent image quality at 3 T. These results, however, must be confirmed by further studies involving larger groups.

Conflict of interest

None.

References

[1] Vitellas KM, El-Dieb A, Vaswani KK, et al. MR cholangiopancreatography in patients with primary sclerosing cholangitis: interobserver variability and comparison with endoscopic retrograde cholangiopancreatography. Am J Roentgenol 2002;179:399–407.
[2] Aube C, Delorme B, Yzet T, et al. MR cholangiopancreatography versus endoscopic sonography in suspected common bile duct lithiasis: a prospective, comparative study. Am J Roentgenol 2005;184:55–62.
[3] Hoeffel C, Azizi L, Lewin M, et al. Normal and pathologic features of the postoperative biliary tract at 3D MR cholangiopancreatography and MR imaging. Radiographics 2006;26:1603–20.
[4] Watanabe Y, Nagayama M, Okumura A, et al. MR imaging of acute biliary disorders. Radiographics 2007;27:477–95.
[5] Masselli G, Gualdi G. Hilar cholangiocarcinoma: MRI/MRCP in staging and treatment planning. Abdom Imaging 2008;33:441–51.
[6] Limanond P, Raman SS, Ghobrial RM, Busuttil RW, Lu DS. The utility of MRCP in preoperative mapping of biliary anatomy in adult-to-adult living related liver transplant donors. J Magn Reson Imaging 2004;19:209–15.
[7] Merkle EM, Haugan PA, Thomas J, Jaffe TA, Gullotto C. 3.0- versus 1.5-T MR cholangiography: a pilot study. Am J Roentgenol 2006;186:516–21.
[8] Safar F, Kamura T, Okamuto K, Sasai K, Gejyo F. Magnetic resonance T1 gradient-echo imaging in hepatolithiasis. Abdom Imaging 2005;30:297–302.
[9] Lee VS, Morgan GR, Teperman LW, et al. MR imaging as the sole preoperative imaging modality for right hepatectomy: a prospective study of living adult-to-adult liver donor candidates. Am J Roentgenol 2001;176:1475–82.
[10] Limanond P, Raman SS, Ghobrial RM, Busuttil RW, Saab S, Lu DS. Preoperative imaging in adult-to-adult living related liver transplant donors: what surgeons want to know. J Comput Assist Tomogr 2004;28:149–57.
[11] Schick F. Whole-body MRI at high field: technical limits and clinical potential. Eur Radiol 2005;15:946–59.
[12] Merkle EM, Dale BM. Abdominal MRI at 3.0 T: the basics revisited. Am J Roentgenol 2006;186:1524–32.
[13] O'Regan DP, Fitzgerald J, Allsop J, et al. A comparison of MR cholangiopancreatography at 1.5 and 3.0 Tesla. Br J Radiol 2005;78:894–8.
[14] Isoda H, Kataoka M, Maetani Y, et al. MRCP imaging at 3.0 T vs. 1.5 T: preliminary experience in healthy volunteers. J Magn Reson Imaging 2007;25:1000–6.
[15] Lichy MP, Wietek BM, Mugler III JP, et al. Magnetic resonance imaging of the body trunk using a single-slab, 3-dimensional, T2-weighted turbo-spin-echo sequence with high sampling efficiency (SPACE) for high spatial resolution imaging: initial clinical experiences. Invest Radiol 2005;40:754–60.
[16] Weigel M, Hennig J. Contrast behavior and relaxation effects of conventional and hyperecho-turbo spin echo sequences at 1.5 and 3 T. Magn Reson Med 2006;55:826–35.
[17] Haystead CM, Dale BM, Merkle EM. N/2 ghosting artifacts: elimination at 3.0-T MR cholangiography with SPACE pulse sequence. Radiology 2008;246:589–95.
[18] Arizono S, Isoda H, Maetani YS, et al. High spatial resolution 3D MR cholangiography using high sampling efficiency technique (SPACE) at 3 T: comparison with conventional constant flip angle sequence in healthy volunteers. J Magn Reson Imaging 2008;28:685–90.
[19] Schindera ST, Miller CM, Ho LM, DeLong DM, Merkle EM. Magnetic resonance (MR) cholangiography: quantitative and qualitative comparison of 3.0 Tesla with 1.5 Tesla. Invest Radiol 2007;42:399–405.
[20] Barth MM, Smith MP, Pedrosa I, Lenkinski RE, Rofsky NM. Body MR imaging at 3.0 T: understanding the opportunities and challenges. Radiographics 2007;27:1445–64.
[21] Yeh BM, Breiman RS, Taouli B, Qayyum A, Roberts JP, Coakley FV. Biliary tract depiction in living potential liver donors: comparison of conventional MR, mangafodipir trisodium-enhanced excretory MR, and multi-detector row CT cholangiography—initial experience. Radiology 2004;230:645–51.
[22] Schroeder T, Malago M, Debatin JF, Goyen M, Nadalin S, Ruehm SG. All-in-one imaging protocols for the evaluation of potential living liver donors: comparison of magnetic resonance imaging and multidetector computed tomography. Liver Transpl 2005;11:776–87.
[23] Schroeder T, Radtke A, Kuehl H, Debatin JF, Malago M, Ruehm SG. Evaluation of living liver donors with an all-inclusive 3D multi-detector row CT protocol. Radiology 2006;238:900–10.

nature chemistry

ARTICLES

PUBLISHED ONLINE: 23 SEPTEMBER 2009 | DOI: 10.1038/NCHEM.365

Self-assembling nanoprobes that display off/on ^{19}F nuclear magnetic resonance signals for protein detection and imaging

Yousuke Takaoka[1], Takashi Sakamoto[1], Shinya Tsukiji[1,4], Michiko Narazaki[2], Tetsuya Matsuda[2], Hidehito Tochio[3], Masahiro Shirakawa[3] and Itaru Hamachi[1,4]*

Magnetic resonance imaging (MRI) is one of the most promising techniques for the non-invasive visualization of biomarkers and biologically relevant species, both *in vivo* and *ex vivo*. Although ^{1}H MRI with paramagnetic contrast agents, such as Gd^{3+} complexes and iron oxide, is widely used, it often suffers from low contrast because of the large background signals caused by the abundant distribution of protons in biological samples. Here we report the use of supramolecular organic nanoparticles to detect specific proteins by ^{19}F-based MRI in an off/on mode. In NMR spectroscopy these designed probes are silent when aggregated, but in the presence of a target protein they disassemble to produce a sharp signal. This 'turn-on' response allowed us to visualize clearly the protein within live cells by ^{19}F MRI and construct an in-cell inhibitor assay. This recognition-driven disassembly of nanoprobes for a turn-on ^{19}F signal is unprecedented and may extend the use of ^{19}F MRI for specific protein imaging.

MRI is superior to optical bioimaging in living systems for the visualization of deep tissues[1–3]. Currently, ^{1}H MRI is widely used for diagnostic purposes because it is highly sensitive, which is attributed to the abundance of water molecules in the vicinity of contrast agents. However, ^{1}H MRI also often suffers from low contrast-to-noise ratio because of the large background signals from water protons. Therefore, for the specific imaging of biomarkers and biologically relevant molecules with higher functional and/or spatial resolution, both *in vivo* and *ex vivo*, there is still an obvious need to develop new methodologies.

Several approaches have been proposed[2–6]. In particular, ^{19}F holds great promise as an alternative nuclide for MRI as it is highly sensitive in nuclear magnetic resonance (NMR) spectroscopy (83% relative to ^{1}H) and has 100% natural abundance. A more important advantage of ^{19}F is that in animal bodies essentially no ^{19}F is detectable by NMR spectroscopy, which therefore eliminates interference from background signals[7,8]. As such, when a probe containing ^{19}F is applied to a biological sample, only the signal from the molecule can be detected. However, ^{19}F MRI technology is still in its infancy. Despite the significant importance for medical diagnosis, strategies to image specific proteins and/or enzymes with high MRI contrast are very limited.

To date, both targeting and switching probes have been proposed for ^{19}F NMR–MRI detection. The former is based on the accumulation of probes in specific regions in tissues through binding to localized components[9], and the latter provides signals that can be modulated by enzymatic reaction. Two types of switching ^{19}F MRI probes reported involve enzyme substrates: one displays chemical shift changes[10] and the other shows a signal turn-on dependent on paramagnetic relaxation enhancement on enzymatic cleavages[11]. The switching of these probes relies entirely on the catalytic activity of the enzymes, and thus the probes are spatially diffused away from the target enzyme and also not applicable for non-enzymatic protein targets. Therefore, more universal MRI strategies for protein detection and imaging that do not rely on enzymatic activities are highly desirable.

Here we describe a novel strategy to detect specific proteins with an 'off/on' type of signal in ^{19}F NMR spectroscopy using dynamic self-assembled nanoparticles. The basis of our idea is that the ^{19}F NMR signal is broadened and attenuated when the molecules assemble into aggregates of high molecular mass (M_r), but recovers on their disassembly. ^{19}F has a relatively large chemical shift anisotropy (approximately 39 ppm for a $-CF_3$ group)[12], so the transverse relaxation of signals in ^{19}F NMR spectroscopy is extremely sensitive to the apparent M_r because of the relaxation mechanism of chemical shift anisotropy. Thus, the formation of a large molecular assembly can cause severe broadening of the signal in ^{19}F NMR spectroscopy. Accordingly, small-molecule probes were designed that are composed of a ^{19}F-containing group and a ligand specific to the protein of interest, and concurrently equipped with the ability to form nanoaggregates. The probe alone is NMR-silent because of its self-assembly, but gives a distinct ^{19}F signal in response to the target protein through the binding-mediated disassembly of the probe (Fig. 1a). As the signal response is determined by specific protein–ligand interactions, this principle should be applicable to the detection of certain proteins, including both enzymes and non-enzymatic proteins.

For the proof-of-principle experiment, we initially chose human carbonic anhydrase I (hCAI) as a target protein. Probe **1** was synthesized to give a 3,5-bis(trifluoromethyl)benzene derivative that carries six magnetically equivalent ^{19}F nuclei connected to a benzenesulfonamide moiety, a ligand specific for hCAI (dissociation

[1]Department of Synthetic Chemistry and Biological Chemistry, Graduate School of Engineering, Kyoto University, Katsura, Nishikyo-ku, Kyoto 615-8510, Japan, [2]Department of Systems Science, Graduate School of Informatics, Kyoto University, 36-1 Yoshida-Honmachi, Sakyo-ku, Kyoto 606-8501, Japan, [3]Department of Molecular Engineering, Graduate School of Engineering, Kyoto University, Katsura, Nishikyo-ku, Kyoto 615-8510, Japan, [4]Core Research for Evolutional Science and Technology, Japan Science and Technology Agency, Sanbancho, Chiyodaku, Tokyo, 102-0075, Japan.
*e-mail: ihamachi@sbchem.kyoto-u.ac.jp

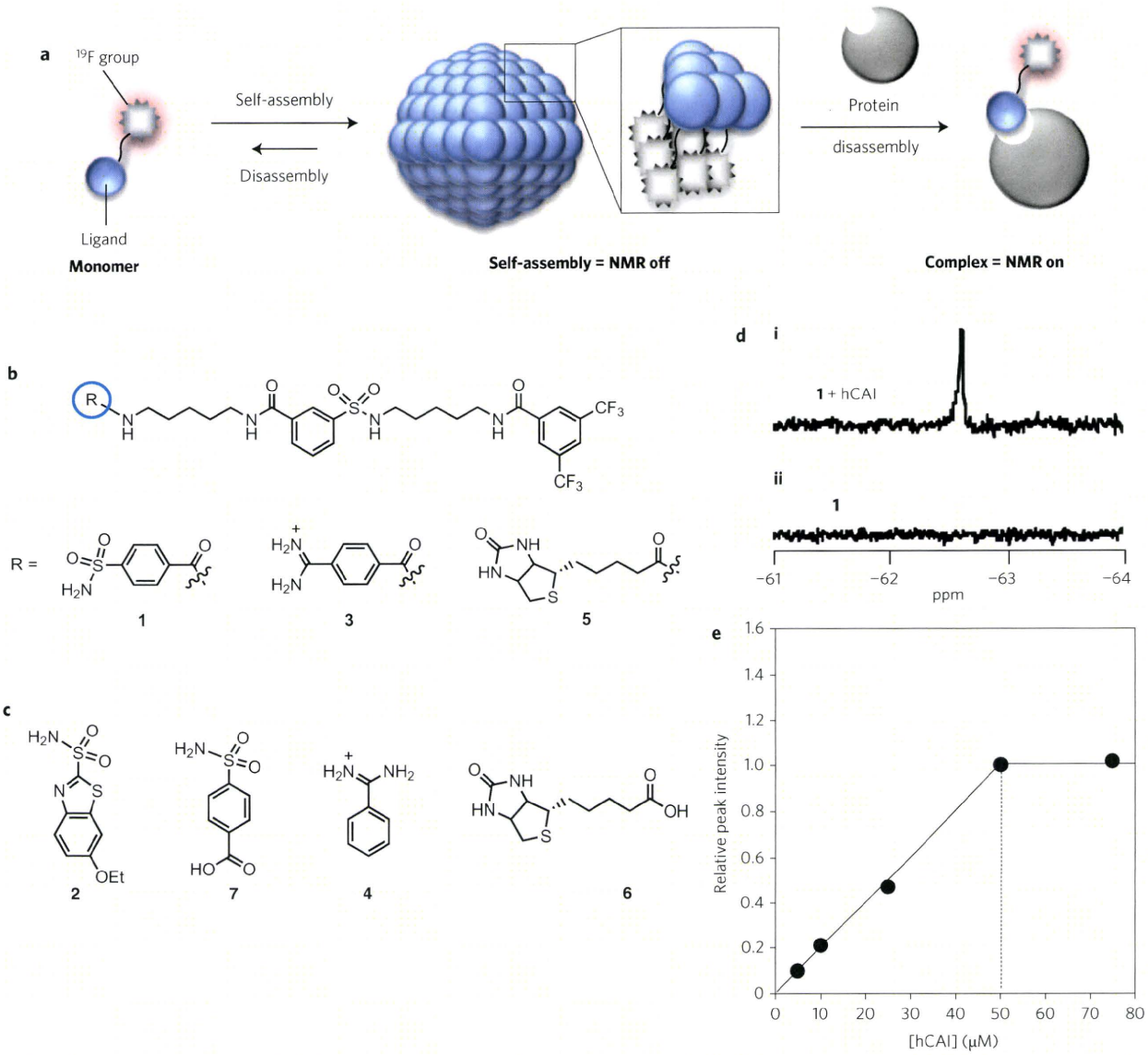

Figure 1 | Off/on ^{19}F NMR probes for protein imaging. a, Strategy used for an off/on switching mode of ^{19}F NMR. **b**, Chemical structures of probes **1**, **3** and **5** for hCAI, TPS and avidin, respectively. **c**, Chemical structures of enzyme inhibitors **2** and **7** for hCAI, **4** for TPS and ligand **6** for avidin. **d**, Turn-on ^{19}F NMR signal of probe **1** (50 μM) in the presence (**i**) or absence (**ii**) of hCAI (50 μM). The signal-to-noise ratio (SNR) was 60.1. **e**, Dependence of the ^{19}F-signal intensity (−62.6 ppm) on the hCAI concentration for probe **1** (50 μM) in 50 mM HEPES buffer (pH 7.2, 0.2 mM TFA as an internal standard for peak intensity and chemical shift, 10% D_2O (v/v)) at 25 °C.

constant K_d = ca. 3 μM) (ref. 13), by a relatively hydrophobic linker (Fig. 1b and Supplementary Information). When **1** was dissolved in a buffer solution that contained trifluoroacetic acid (TFA; internal standard at −75.6 ppm), no ^{19}F signal was observed. However, a sharp signal appeared at −62.6 ppm on the addition of hCAI (Fig. 1d). The signal intensity increased linearly in proportion to the concentration of hCAI, and was saturated at a 1:1 molar ratio of probe **1** and hCAI (Fig. 1e). On the subsequent addition of a strong inhibitor, ethoxzolamide (**2**, Fig. 1c)[14], into the above solution, the signal disappeared again (Supplementary Fig. 1a). These data indicate that (1) probe **1** alone is silent in NMR spectroscopy, (2) the ^{19}F signal can be assigned to probe **1** bound to the ligand-binding pocket of hCAI and (3) the signal can be turned off in a reversible manner when the probe is expelled from the protein (that is, when the target protein is incapable of binding the probe).

We next examined the target specificity of probe **1** under miscellaneous conditions. The addition of **1** to a mixture of four proteins different from hCAI effectively (haemoglobin, bovine serum albumin, concanavaline A and chymotrypsin) did not give a sharp signal. However, the ^{19}F signal was observed clearly in a mixture that contained the four proteins and hCAI (Supplementary Fig. 1b). We also found that the hCAI-induced appearance of the ^{19}F signal occurred with a 70% fetal bovine serum solution, which contains many biological substances, including proteins, lipids and small molecules (Supplementary Fig. 1c). Overall, these results clearly demonstrate that probe **1** can detect hCAI selectively by a turn-on ^{19}F signal, even in crude samples.

The self-assembly/disassembly properties of probe **1** were investigated with various techniques. Atomic force microscopy (AFM) was used to observe spherical or oval aggregates of **1** with a size that ranged from 200 to 500 nm in diameter (Fig. 2a). Transmission electron microscopy (TEM) and scanning electron microscopy (SEM) data showed the formation of aggregates of approximately 200 nm in size (Fig. 2b and Supplementary Fig. 2a). The ultraviolet–visible absorption spectrum of **1** in a buffer solution showed a broad visible-light scattering around 500–700 nm because

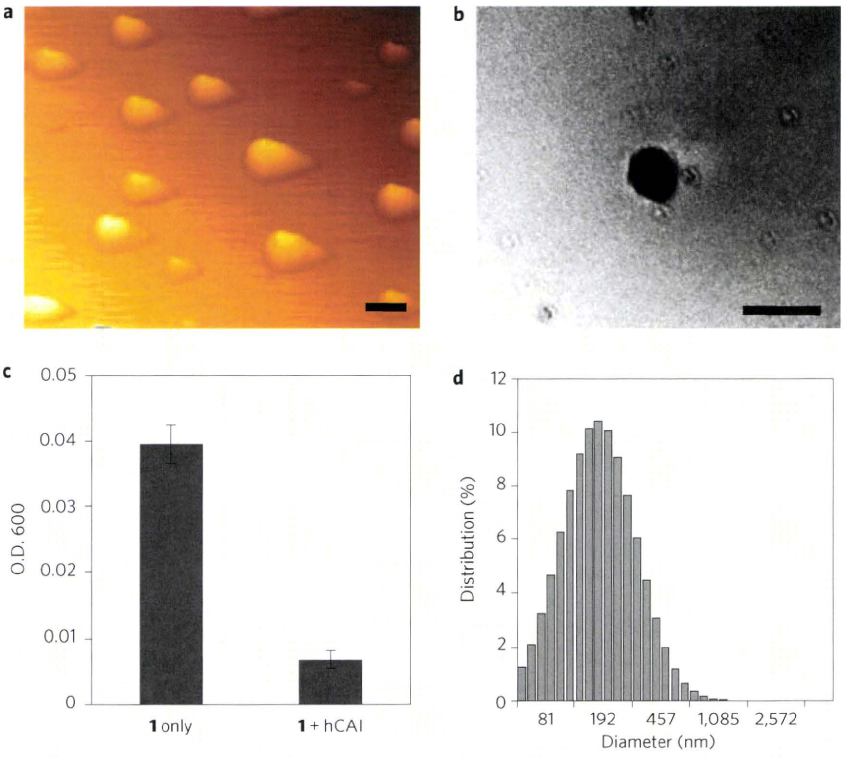

Figure 2 | Microscopic and spectroscopic characterization of the self-assembled nanoparticles of probe 1. a, AFM image of the self-assembled probe **1** (25 μM) (scale bar 500 nm). **b**, TEM image of the self-assembled probe **1** (25 μM) (scale bar 500 nm). **c**, Optical density (O.D.) at 600 nm of an aqueous solution that contained probe **1** (25 μM) in the absence or presence of hCAI (25 μM). Experiments were performed in triplicate to obtain mean and standard deviation values (shown as error bars). **d**, DLS analysis of particle-size distribution of the self-assembled probe **1** (25 μM). All experiments were performed in 50 mM HEPES buffer (pH 7.2, 0.2 mM TFA).

of the aggregates of **1** (Fig. 2c and Supplementary Fig. 2b). The scattering decreased tenfold with the addition of hCAI, which indicates that hCAI collapsed the aggregates. Dynamic light scattering (DLS) measurements in buffer solution that contained **1** alone consistently showed aggregates with a diameter of mean size 250 nm (Fig. 2d), whereas negligible DLS intensity was obtained after adding hCAI to the solution. The M_r of the nanoaggregate of **1** was estimated from the observed diameter to be roughly 10^7 Da, and that of the complex between hCAI and probe **1** to be 3×10^4 Da. We thus conclude that the binding of probe **1** to hCAI induces the disassembly of the nanoaggregates, which dramatically decreases the apparent M_r. This decrease effectively reduces the ^{19}F relaxation rate, so that a sharp ^{19}F signal is observed. From the concentration dependency of DLS measurements, the critical aggregation concentration of the self-assembly of **1** was found to be <5 μM (Supplementary Fig. 2c).

On the basis of this, we next produced a turn-on ^{19}F probe, **3**, for trypsin (TPS). Instead of benzenesulfonamide, benzamidine (**4**), a typical inhibitor for TPS (K_d = ca. 20 μM (ref. 15)), was linked to the 3,5-bis(trifluoromethyl)benzene moiety as a suitable ligand. In NMR spectroscopy, almost no signal was detected in the buffer solution that contained probe **3** alone, whereas a new signal was intensified on the addition of TPS (Fig. 3a). In the presence of **4** (Fig. 1c), such signal intensification did not occur. Similarly, with ^{19}F NMR spectroscopy the biotin-tethered probe **5** showed a clear off/on response to a non-enzymatic protein, avidin (Fig. 3b) (K_d of (+)-biotin (**6**), ca. 10^{-15} M (ref. 16)). Furthermore, the orthogonality of probes **1** and **5** was investigated. It was shown that **1** responded to hCAI, but not to avidin, and vice versa for **5** (Supplementary Fig. 3). These data demonstrate the general applicability of this strategy to the design of turn-on supramolecular nanoprobes to detect target proteins by ^{19}F NMR spectroscopy.

Notably, probe **1** was also capable of detecting hCA within live cells. hCA is a cytosolic protein and naturally expressed within human red blood cells (RBCs) at a concentration of approximately 170 μM (ref. 17). A suspension of RBCs was incubated with **1** for a few minutes and, after collecting cells, in-cell ^{19}F NMR spectroscopy was conducted. Note that no haemolysis occurred during the experiments. A signal was clearly observed at −62.6 ppm (Fig. 4a, spectrum **i**), a chemical shift identical to that obtained using purified hCAI and **1** (Fig. 1d), although there was a slight peak broadening. In contrast, no signal appeared when **1** was incubated with RBCs in

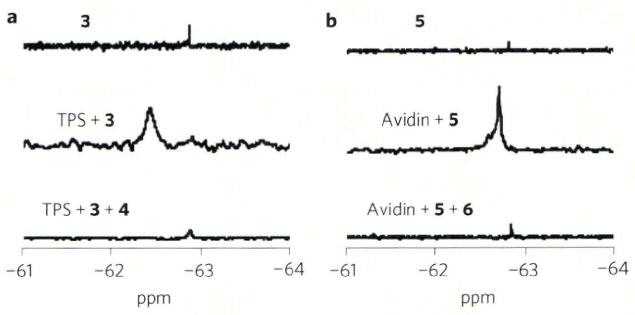

Figure 3 | Turn-on ^{19}F NMR detection of TPS and avidin by probes 3 and 5, respectively. a, ^{19}F NMR spectra of **3** (100 μM) alone, in the presence of TPS (50 μM) and in the presence of both TPS and **4** (500 μM) in 50 mM tris-HCl buffer (pH 8.5, 0.2 mM TFA, 300 mM NaCl, 10% D_2O (v/v)). The SNR was 12.2. **b**, ^{19}F NMR spectra of **5** (100 μM) alone, in the presence of avidin (50 μM) and in the presence of both avidin and **6** (500 μM) in 50 mM HEPES buffer (pH 7.2, 0.2 mM TFA, 500 mM NaCl, 10% D_2O (v/v)). The SNR was 57.3.

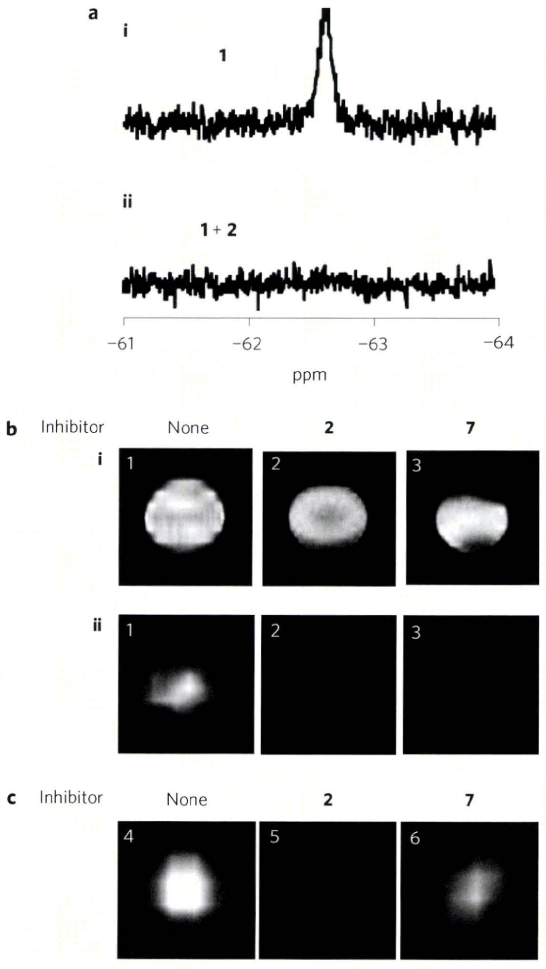

Figure 4 | ^{19}F NMR spectra and magnetic resonance images in RBCs. **a**, ^{19}F NMR spectra of probe **1** in the absence (**i**) or presence (**ii**) of **2** in RBCs. The SNR was 14.2. **b**, Magnetic resonance images (**i**, ^{1}H; **ii**, ^{19}F) of probe **1** in a test tube. **c**, Magnetic resonance images of probe **1** in RBCs. Conditions for samples 1-3: **1** (100 μM), hCAI (50 μM), inhibitors (**2** or **7**) (0 or 500 μM) in 50 mM HEPES buffer (pH 7.2, 0.2 mM TFA). Conditions for samples 4-6: a solution of probe **1** (200 μM) and inhibitors (0 or 1 mM) in 2 ml HEPES buffer saline (20 mM HEPES, 107 mM NaCl, 6 mM KCl, 1.2 mM $MgSO_4$, 2 mM $CaCl_2$, 11.5 mM glucose, pH 7.4) was added to a 2.5 ml RBC suspension. For all samples, after centrifugation the supernatant was removed and the sedimented RBCs were resuspended in 50 mM HEPES buffer (pH 7.2, 100 mM NaCl, 0.17 mM TFA, 20% D_2O (v/v)) and subjected to NMR or MRI measurements at 25 °C.

the presence of **2** (Fig. 4a, spectrum **ii**). Clearly, probe **1** is cell-permeable and can detect endogenous hCA specifically with the turn-on signal response, even within cells.

Turn-on probe **1** allowed us to visualize the target protein using a ^{19}F MRI phantom. At first, ^{1}H and ^{19}F magnetic resonance images were acquired after mixing hCAI with probe **1** under test-tube conditions in the absence (sample 1) and presence (sample 2) of inhibitor **2** or 4-sulfamoylbenzoic acid[13] (**7**, Fig. 1c) (sample 3). In ^{1}H MRI, all three samples gave indistinguishable images (Fig. 4b, image **i**). However, a distinct ^{19}F magnetic resonance image was obtained from sample 1, whereas no signal was detected in samples 2 and 3 (Fig. 4b, image **ii**). These results are consistent with the ^{19}F NMR spectroscopic data described above (Fig. 1d and Supplementary Fig. 1a). More significantly, a clear ^{19}F magnetic resonance image was observed with sample 4, which contained RBCs and probe **1** (Fig. 4c). The magnetic resonance image was diminished totally by co-incubation of **2** (sample 5), which confirms that the positive magnetic resonance image obtained is, indeed, because probe **1** was bound to hCAI within the cells. Interestingly, sample 6, which contained RBCs, probe **1** and **7**, still gave a magnetic resonance image similar to that of sample 4, despite the presence of the inhibitor. Given that **7** efficiently blocks the binding of probe **1** to hCAI under test-tube conditions (Fig. 4b, image **ii**), this result is reasonably ascribed to the lower cell-membrane permeability of anionic **7** compared with that of neutral **2**. Therefore, this system serves as a cell-based inhibitor-screening platform that can visualize the potency of inhibitors in cellular contexts.

Conclusions

In conclusion, we have developed supramolecular ^{19}F-containing nanoprobes that can detect specific proteins spatially by a ^{19}F MRI technique with a sharp turn-on/off switching. The simple principle for the off/on response (that is, self-assembly and recognition-driven disassembly of the nanoprobe[18]) should be applicable to the design of other turn-on probes for various target proteins by appropriately replacing the ligand module, as shown for TPS probe **3** and avidin probe **5**. Unlike other MRI contrast techniques[1–6,11], this method does not require any metals that have potential toxicity. From a practical viewpoint, the sensitivity of ^{19}F MRI is considerably lower than that of ^{1}H MRI and thus this system is not yet sufficient for *in vivo* or clinical application using conventional bench-top spectrometers (which, generally, have strengths of ~1 tesla). Functional ^{19}F probes are also very limited in number. However, we believe that, with further advances in both instrumentation and chemistry, a ^{19}F-based NMR–MRI technique may become a more powerful modality, both in practical diagnosis and in basic research. It is essential for chemists to establish general and useful design concepts for new ^{19}F probes that facilitate functional and molecular MRI.

Methods

^{19}F NMR spectroscopy of probe 1 with various concentrations of hCAI. hCAI (5.0 mg) was dissolved in 50 mM HEPES buffer (1.0 ml, pH 7.2, 10% D_2O (v/v), 0.2 mM TFA). The concentration of hCAI was determined by absorbance at 280 nm using the molar extinction coefficient (49,000 M^{-1} cm^{-1}) (ref. 19) and a 100 μM stock solution was prepared. Probe **1** (3.0 mg, 3.8 μmol) was dissolved in 75 μl of dimethylsulfoxide (DMSO) as the stock solution, and slowly added to the hCAI solution (0.6% DMSO (v/v)). These samples were analysed by ^{19}F NMR spectroscopy with TFA as an internal standard (−75.6 ppm) (Supplementary Methods).

Atomic force microscopy, transmission electron microscopy and scanning electron microscopy observations. In AFM imaging, a solution of probe **1** was spin-coated onto a freshly cleaved mica surface and dried *in vacuo*. Images of the sample were obtained with a tapping-mode AFM on a SEIKO SPA-400 microscope. In TEM imaging, a solution of probe **1** was deposited on a thin carbon-support film and dried *in vacuo*. Images of the sample were obtained with a JEOL JEM-1025 microscope, operating at 100 kV, without any contrast agent. In SEM imaging, a solution of probe **1** was deposited on a silicon wafer and dried *in vacuo*. Images of the sample were obtained with a JEOL JFC-1600 microscope, operating at 15 kV, with the addition of platinum spray as a conductive material.

Measurements of optical density and dynamic light scattering. The optical density was measured at 25 °C in 50 mM HEPES buffer (pH 7.2, 0.2 mM TFA) using a quartz cell (1 cm). The DMSO stock solution of probe **1** was slowly added to the buffer solution (0.6% DMSO (v/v)) to give 25 μM. The measurements of DLS were performed under the same conditions with a tubular-type cell. All measurements were performed in triplicate.

^{19}F NMR spectroscopy of probe 3 and probe 5. TPS (5.0 mg) was dissolved in 50 mM tris-HCl buffer (1.0 ml, pH 8.5, 300 mM NaCl, 0.2 mM TFA, 10% D_2O (v/v)). The concentration of TPS was determined by the absorbance at 280 nm using the molar extinction coefficient (36,700 M^{-1} cm^{-1}) (ref. 20) and a 100 μM stock solution was prepared. Probe **3** (1.0 mg, 1.3 μmol) was dissolved in 26 μl of DMSO and 26 μl of 50 mM tris-HCl buffer (pH 8.5) as the stock solution (25 mM), and slowly added to the TPS solution (0.2% DMSO (v/v)). Avidin (5.0 mg) was dissolved in 50 mM HEPES buffer (1.0 ml, pH 7.2, 500 mM NaCl, 0.2 mM TFA, 10% D_2O (v/v)). The concentration of avidin was determined by the absorbance at 280 nm using the molar extinction coefficient (35,700 M^{-1} cm^{-1}) (ref. 21) and 100 μM stock solution was prepared. Probe **5** (3.0 mg, 3.8 μmol) was dissolved in 72 μl of DMSO as the stock solution, and slowly added to the avidin solution

(0.6% DMSO (v/v)). Conditions used for ^{19}F NMR spectroscopy were the same as those used for probe **1**.

Assays of hCA inhibitor in red blood cells. A 2 ml solution of probe **1** (200 μM) and inhibitor (**2**, 0 or 1 mM, or **7**, 0 or 1 mM) in HEPES buffer saline (20 mM HEPES, 107 mM NaCl, 6 mM KCl, 1.2 mM $MgSO_4$, 2 mM $CaCl_2$, 11.5 mM glucose, pH 7.4) was added to 2 ml of sedimented RBCs, and the suspension was incubated at room temperature for a few minutes. After centrifugation (1,500 revolutions per minute for five minutes), the supernatant was removed and re-suspended in buffer (50 mM HEPES buffer (pH 7.2), 100 mM NaCl, 0.17 mM TFA, 20% D_2O (v/v)) for ^{19}F NMR spectroscopy. 0.7 ml and 2.5 ml of the suspension were used for ^{19}F NMR spectroscopy and MRI, respectively, at 25 °C.

^{1}H and ^{19}F MRI in test tubes or in RBCs. ^{1}H magnetic resonance images of samples 1–3 (in test tubes) were obtained by gradient-spin echo with repetition time (TR)/echo time (TE) = 100/6 ms, flip angle = 30°, field of view (FOV) = 16 × 4 cm, slice thickness = 5 mm, matrix size = 256 × 256 and the number of accumulation (NA) = 1. ^{19}F magnetic resonance images of sample 1–3 (in test tubes) were obtained by fast-spin echo with TR/TE = 1,500/5.5 ms, echo train length = 32, FOV = 16 × 4 cm without slice selection, matrix size = 128 × 32, depth of sample tube = 20 mm, voxel size ~31 mm^3 and NA = 1,200. ^{19}F magnetic resonance images of samples 4–6 (in RBCs) were obtained by gradient-spin echo with TR/TE = 1,000/2.4 ms, flip angle = 90°, FOV = 32 × 8 cm without slice selection, matrix size = 128 × 32, depth of sample tube = 30 mm, voxel size ~188 mm^3 and NA = 400. The sine window function was applied to the ^{19}F magnetic resonance images. All the images were acquired at 25 °C.

Received 14 April 2009; accepted 6 August 2009; published online 23 September 2009

References

1. Kiessling, F., Morgenstern, B. & Zhang, C. Contrast agents and applications to assess tumor angiogenesis *in vivo* by magnetic resonance imaging. *Curr. Med. Chem.* **14,** 77–91 (2007).
2. Perez, J. M., Josephson, L., O'Loughlin, T., Högemann, D. & Weissleder, R. Magnetic relaxation switches capable of sensing molecular interactions. *Nature Biotechnol.* **20,** 816–820 (2002).
3. Louie, A. Y. *et al. In vivo* visualization of gene expression using magnetic resonance imaging. *Nature Biotechnol.* **18,** 321–325 (2000).
4. Sosnovik, D. E. & Weissleder, R. Emerging concepts in molecular MRI. *Curr. Opin. Biotech.* **18,** 4–10 (2007).
5. Woods, M., Woessner, D. E. & Sherry A. D. Paramagnetic lanthanide complexes as PARACEST agents for medical imaging. *Chem. Soc. Rev.* **35,** 500–511 (2006).
6. Jun, Y., Lee, J-H. & Cheon, J. Chemical design of nanoparticle probes for high-performance magnetic resonance imaging. *Angew. Chem. Int. Ed.* **47,** 5122–5135 (2008).
7. Danielson, M. A. & Falke, J. J. Use of ^{19}F NMR to probe protein structure and conformational changes. *Annu. Rev. Biophys. Biomol. Struct.* **25,** 163–195 (1996).
8. Yu, J., Kodibagkar, V. D., Cui, W. & Mason, R. P. ^{19}F: a versatile reporter for non-invasive physiology and pharmacology using magnetic resonance. *Curr. Med. Chem.* **12,** 819–848 (2005).
9. Higuchi, M. *et al.* ^{19}F and ^{1}H MRI detection of amyloid β plaques *in vivo*. *Nature Neurosci.* **8,** 527–533 (2005).
10. Yu, J., Liu, L., Kodibagkar, V. D., Cui, W. & Mason, R. P. Synthesis and evaluation of novel enhanced gene reporter molecules: detection of β-galactosidase activity using ^{19}F NMR of trifluoromethylated aryl β-D-garactopyranosides. *Bioorg. Med. Chem.* **14,** 326–333 (2006).
11. Mizukami, S. *et al.* Paramagnetic relaxation-based ^{19}F MRI probe to detect protease activity. *J. Am. Chem. Soc.* **130,** 794–795 (2008).
12. Grage, S. L. *et al.* Solid state ^{19}F NMR parameters of fluorine-labeled amino acids. Part II: Aliphatic substituents. *J. Magn. Reson.* **191,** 16–23 (2008).
13. Taylor, P. W., King, R. W. & Burgen, A. S. V. Kinetics of complex formation between human carbonic anhydrases and aromatic sulfonamides. *Biochemistry* **9,** 2638–2645 (1970).
14. Casini, A. *et al.* Carbonic anhydrase inhibitors: SAR and X-ray crystallographic study for the interaction of sugar sulfamates/sulfamides with isozymes I, II and IV. *Bioorg. Med. Chem. Lett.* **13,** 841–845 (2003).
15. Talhout, R., Villa, A., Mark, A. E. & Engberts, J. B. F. N. Understanding binding affinity: a combined isothermal titration calorimetry/molecular dynamics study of the binding of a series of hydrophobically modified benzamidinium chloride inhibitors to trypsin. *J. Am. Chem. Soc.* **125,** 10570–10579 (2003).
16. Green, N. M. The use of [^{14}C]biotin for kinetic studies and for assay. *Biochem. J.* **89,** 585–591 (1963).
17. Casey, J. R. *et al.* Carbonic anhydrase inhibitors. Design of selective, membrane-impermeant inhibitors targeting the human tumor-associated isozyme IX. *J. Med. Chem.* **47,** 2337–2347 (2004).
18. Savariar, E. N., Ghosh, S. González, D. C. & Thayumanavan, S. Disassembly of noncovalent amphiphilic polymers with proteins and utility in pattern sensing. *J. Am. Chem. Soc.* **130,** 5416–5417 (2008).
19. Chazalette, C. *et al.* Carbonic anhydrase inhibitors. Design of anticonvulsant sulfonamides incorporating indane moieties. *Bioorg. Med. Chem. Lett.* **14,** 5781–5786 (2004).
20. Talhout, R. & Engberts, J. B. F. N. Thermodynamic analysis of binding of *p*-substituted benzamidines to trypsin. *Eur. J. Biochem.* **268,** 1554–1560 (2001).
21. Finn, F. M., Titus, G., Montibeller, J. A. & Hofmann, K. Hormone-receptor studies with avidin and biotinylinsulin–avidin complexes. *J. Biol. Chem.* **255,** 5742–5746 (1980).

Acknowledgements

We thank E. Ashihara (Kyoto University Hospital) for the blood samples, J. Miyake and T. Kunita (Kyoto University) for help with AFM and SEM measurements. Y.T. acknowledges the JSPS Research Fellowships for Young Scientists. This work was partly supported by CK integrated Medical Bio-imaging Project (MEXT) and by CREST (Japan Science and Technology Agency).

Author contributions

I.H. conceived the project. Y.T., T.S., S.T. and I.H. designed the experiments. Y.T. performed all the experiments, with help from H.T. and M.S. on ^{19}F NMR measurements. M.N. and T.M. performed the MRI experiments. The manuscript was written by Y.T., S.T. and I.H., and edited by all the co-authors.

Additional information

Supplementary information and chemical compound information accompany this paper at www.nature.com/naturechemistry. Reprints and permission information is available online at http://npg.nature.com/reprintsandpermissions/. Correspondence and requests for materials should be addressed to I.H.

J|A|C|S COMMUNICATIONS

Published on Web 10/20/2009

Monitoring of Biological One-Electron Reduction by ^{19}F NMR Using Hypoxia Selective Activation of an ^{19}F-Labeled Indolequinone Derivative

Kazuhito Tanabe,*,† Hiroshi Harada,‡,§ Michiko Narazaki,|| Kazuo Tanaka,⊥ Kenichi Inafuku,⊥ Hirokazu Komatsu,† Takeo Ito,† Hisatsugu Yamada,†,§ Yoshiki Chujo,⊥ Tetsuya Matsuda,|| Masahiro Hiraoka,‡,§ and Sei-ichi Nishimoto*,†

Department of Energy and Hydrocarbon Chemistry, Graduate School of Engineering, Kyoto University, Katsura Campus, Nishikyo-ku, Kyoto 615-8510, Japan, Department of Radiation Oncology and Image-applied Therapy, Graduate School of Medicine, Kyoto University, Shogoin, Sakyo-ku, Kyoto 606-8507, Japan, Nano-Medicine Merger Education Unit, Kyoto University, Shogoin, Sakyo-ku, Kyoto 606-8507, Japan, Department of Systems Science, Graduate School of Informatics, Kyoto University, Yoshida-Honmachi, Sakyo-ku, Kyoto 606-8501, Japan, and Department of Polymer Chemistry, Graduate School of Engineering, Kyoto University, Katsura Campus, Nishikyo-ku, Kyoto 615-8510, Japan

Received June 18, 2009; E-mail: tanabeka@scl.kyoto-u.ac.jp; nishimot@scl.kyoto-u.ac.jp

Intracellular reductases have been closely linked with activation of certain drugs and probes in the tumor-specific microenvironments.[1] Among various enzymes, reductases that catalyze one-electron reduction are involved in the selective activation of functional compounds or materials under hypoxia,[2] a well-known pathophysiological characteristic of solid tumors.[3] Such an enzymatic one-electron reduction has been recognized to be a useful reaction applicable to the design of a tumor hypoxia targeting and imaging strategy. Thus, further quantitative insights into the features of this reaction are important.

Here we demonstrate probing of the biological one-electron reduction of a fluorine (F)-labeled indolequinone (IQ) derivative by ^{19}F NMR that gave us straightforward molecular information even under complicated biological reduction conditions due to low concentrations of endogenous F atoms and the absence of interference with proton signals.[4−6] The family of IQ compounds is well characterized to be superior substrates for several reductases expressed in tumor cells and readily undergoes enzymatic one-electron reduction under hypoxic conditions. Consequently, IQ derivatives have been employed to develop bioreductive prodrugs and imaging probes targeting tumor hypoxia[7,8] that are efficiently activated by endogenous reductase to release a given functional component selectively under hypoxic conditions. We prepared an ^{19}F NMR signal supplier (IQ-F) consisting of a hypoxia-sensitive IQ parent unit and a nonafluoro-*tert*-butyl group and monitored the change in ^{19}F chemical shift during the bioreduction. One-electron reduction of IQ-F by isolated or intracellular reductase under hypoxic conditions released the nonafluoro-*tert*-butyl alcohol (F-OH) constituent. We observed a new ^{19}F signal due to the resultant F-OH at a characteristic chemical shift, which differed from that of IQ-F. In contrast, the release of F-OH was efficiently suppressed upon addition of O_2 and thereby the corresponding signal failed to appear. Kinetic studies indicated that O_2 prevented to a lesser extent the binding of IQ-F to reductase but decreased the rate of the net reaction due to oxidation of a semiquinone anion radical intermediate generated during the course of the one-electron reduction into the parent IQ-F. In addition, the present reaction could be monitored by chemical shift selective fast spin echo (FSE),[9] leading to visualization of the hypoxia-selective reduction by signal intensity using MR imaging.

† Department of Energy and Hydrocarbon Chemistry.
‡ Department of Radiation Oncology and Image-applied Therapy.
§ Nano-Medicine Merger Education Unit.
|| Department of Systems Science.
⊥ Department of Polymer Chemistry.

IQ-F was synthesized by coupling 3-hydroxymethyl-5-methoxy-1,2-dimethylindole-4,7-dione with F-OH (Scheme S1). We conducted the enzymatic reduction of IQ-F in an Ar-purged aqueous acetonitrile solution by means of NADPH:cytochrome P450 reductase, which catalyzes the one-electron reduction of quinone derivatives to semiquinone anion radicals.[7a] We incubated IQ-F with NADPH:cytochrome P450 reductase and its cofactor β-NADPH under hypoxic conditions. Figure 1 shows the reaction of IQ-F monitored by ^{19}F NMR. The appearance of a single new signal at −73.6 ppm during hypoxic treatment is attributable to the formation of F-OH, as confirmed by reference to authentic sample, while the IQ-F starting compound almost completely disappeared (Figure 1B). These results clearly indicate that IQ-F is activated to release the corresponding alcohol F-OH by enzymatic reduction, thereby causing a change in the ^{19}F NMR spectra. In contrast, upon enzymatic treatment under aerobic conditions, a substantial amount of IQ-F remained to produce a negligible signal attributable to F-OH (Figure 1C). Thus, enzymatic reduction of IQ-F occurred in a hypoxia-selective manner, as can be monitored by ^{19}F NMR.[10]

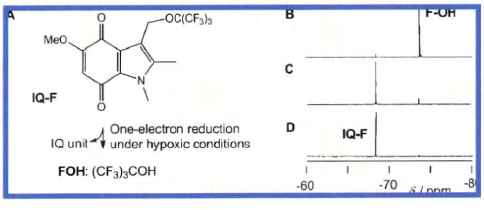

Figure 1. (A) Bioreduction of IQ-F under hypoxic conditions to release F-OH. (B, C, D) One-electron reduction of IQ-F monitored by ^{19}F NMR. IQ-F (0.93 mM) was incubated with NADPH:cytochrome P450 reductase (11.4 μg) and β-NADPH (2 mM) at 37 °C in phosphate buffer; (B) incubated for 15 min under hypoxic conditions; (C) incubated for 15 min under aerobic conditions; and (D) before incubation.

The steady-state kinetic parameters, V_{max} and K_m, for the release of F-OH were derived from a Lineweaver−Burk plot[11] of the integration values evaluated in the ^{19}F NMR spectra (Figure S1). The V_{max} value for F-OH formation under aerobic conditions (0.20 ± 0.04 pmol min^{-1}) was considerably lower than that under hypoxic conditions (3.1 ± 0.2 pmol min^{-1}), while the K_m value obtained from hypoxic treatment (0.41 ± 0.04 mM) was similar to that from aerobic treatment (0.59 ± 0.16 mM). Thus, binding of IQ-F to reductase was slightly affected by the oxygen concentration, while the net reaction rate was dramatically reduced in the presence of O_2. These characteristics are consistent with the conventional mechanism hitherto proposed for IQ

10.1021/ja904953b CCC: $40.75

derivatives. A semiquinone anion radical intermediate is generated under both hypoxic and aerobic conditions by enzymatic one-electron reduction of IQ. The resulting intermediate is subject to oxidization by O_2 to regenerate the original IQ along with the formation of $O_2^{-\bullet}$ under aerobic conditions, leading to significant suppression of the net reaction. The enzymatic activation of IQ-F, which leads to an NMR signal change, is likely to occur substantially under hypoxic conditions.

To better understand the function of IQ-F in living cells, we also assessed the one-electron reduction of IQ-F in a human cell line of lung carcinoma A549 cells that express NADPH:cytochrome P450 reductase in high amounts.[12,13] A549 cells were cultured in the presence of IQ-F for 12 h under hypoxic or aerobic conditions. The culture medium and the cell lysate were individually harvested and subjected to an NMR study. In a similar manner to the treatment of IQ-F with isolated reductase, a signal originating form the formation of F-OH was observed in the medium obtained upon incubation under hypoxic conditions, as shown in Figure 2A. We also confirmed that a weak F-OH signal was produced upon aerobic treatment. In a control experiment, no signal was observed in the corresponding cell lysates independent of oxygen concentrations (Figure S2). Therefore IQ-F most likely penetrates into living cells where it is activated to release F-OH by intracellular reductases in a hypoxic environment, while it is promptly eliminated from cells due to the small size of the molecule, resulting in the low concentration of the intracellular F-signal supplier, which was below the detection limit.

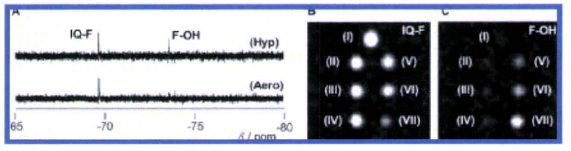

Figure 2. (A) One-electron reduction of IQ-F in A549 cells. A549 cells were incubated with IQ-F (355 μM) for 12 h under hypoxic (Hyp) or aerobic (Aero) conditions. The medium obtained from the reaction sample was subjected to an ^{19}F NMR study. (B,C) ^{19}F MR images of IQ-F incubated with cell lysate of A549 for 0 (I), 6 (II and V), 12 (III and VI), and 24 h (IV and VII) under aerobic (II, III, and IV) or hypoxic (V, VI, and VII) conditions: (B) IQ-F signal selected image; (C) F-OH signal selected image.

To confirm whether the reduction can occur within cells, we further studied the reaction of IQ-F upon treatment with cell lysate. An aqueous solution of IQ-F containing 6% CD_3CN was incubated at 37 °C under hypoxic or aerobic conditions with the lysate of A549 cells. We observed that the ^{19}F NMR signal of F-OH increased in a time-dependent manner only during treatment under hypoxic conditions (Figure S3), indicating that hypoxia-selective one-electron reduction of IQ-F by intracellular reductase is responsible for an exclusive NMR signal change.

In light of the above reaction characteristics of IQ-F, attempts were also made to monitor the reaction of IQ-F by means of MR imaging, a technique widely employed in medical diagnosis.[14] We employed ^{19}F chemical shift selected imaging[9] for probing of the one-electron reduction of IQ-F. IQ-F was incubated under hypoxic and aerobic conditions with the lysate of A549 cells. As shown in Figure 2B and 2C, ^{19}F images of IQ-F and F-OH were obtained individually and simultaneously by FSE with a chemical shift selective pulse.[15] Upon aerobic treatment, an intense IQ-F signal remained, while no F-OH signal was detected even after prolonged incubation. It is striking that the F-OH signal increased with increasing time upon hypoxic treatment, along with a concomitant decrease in IQ-F signals. In accord with the evidence that incubation of IQ-F in a buffer resulted in a similar ^{19}F image as in the sample incubated under aerobic conditions (Figure S5), the hypoxia-selective one-electron reduction of IQ-F could be clearly monitored by ^{19}F MR imaging.

In conclusion, the hypoxia-selective one-electron reduction of IQ-F, which consists of a hypoxia-sensitive IQ parent unit and an ^{19}F signal-transmitting molecular unit of nonafluoro-*tert*-butyl group, was characterized by ^{19}F NMR. During monitoring of the biological reduction of IQ-F, hypoxia-selective activation occurred to induce a chemical shift change of ^{19}F signals attributable to the reductive formation of F-OH. The disappearance of IQ-F to form F-OH could be imaged simultaneously by ^{19}F FSE, thus visualizing the occurrence of the enzymatic one-electron reduction in a hypoxia-selective manner by means of MR imaging.

The one-electron reduction of IQ derivatives has been widely used for hypoxia targeting and imaging. The IQ-F activation system could be applicable to MR imaging of tumor hypoxia. Optimization of the chemical structure of IQ-F derivatives to increase water solubility and intracellular retention and characterization of their pharmacokinetic profiles are now in progress.

Acknowledgment. This work is partly supported by the Innovative Techno-Hub for Integrated Medical Bioimaging Project of the Special Coordination Funds for Promoting Science and Technology, from the Ministry of Education, Culture, Sports, Science and Technology (MEXT), Japan and by the Program for Promotion of Fundamental Studies in Health Sciences of the National Institute of Biomedical Innovation (NIBIO), Japan.

Supporting Information Available: Detail of synthetic protocol and enzymatic reduction of IQ-F. This material is available free of charge via the Internet at http://pubs.acs.org.

References

(1) (a) Chen, Y.; Hu, L. *Med. Res. Rev.* **2009**, *29*, 29. (b) Colucci, M. A.; Moody, C. J.; Couch, G. D. *Org. Biomol. Chem.* **2008**, *6*, 637.
(2) Tanabe, K.; Zhang, Z.; Ito, T.; Hatta, H.; Nishimoto, S. *Org. Biomol. Chem.* **2007**, *5*, 3745.
(3) (a) Kizaka-Kondoh, S.; Inoue, M.; Harada, H.; Hiraoka, M. *Cancer Sci.* **2003**, *94*, 1021. (b) Harris, A. L. *Nat. Rev. Cancer* **2002**, *2*, 38.
(4) (a) Zimmermann, U.; Nöth, U.; Gröhn, P.; Jork, A.; Ulrichs, K.; Lutz, J.; Haase, A. *Artif. Cells, Blood Substitutes, Immobilization Biotechnol.* **2000**, *28*, 129. (b) Yu, J.; Kodibagkar, V. D.; Cui, W.; Mason, R. P. *Curr. Med. Chem.* **2005**, *12*, 819. (c) Higuchi, M.; Iwata, N.; Matsuba, Y.; Sato, K.; Sasamoto, K.; Saido, T. C. *Nat. Neurosci.* **2005**, *8*, 527. (d) Ahrens, E. T.; Flores, R.; Xu, H. Y.; Morel, P. A. *Nat. Biotechnol.* **2005**, *23*, 983.
(5) (a) Tanaka, K.; Kitamura, N.; Naka, K.; Chujo, Y. *Chem. Commun.* **2008**, 6176. (b) Mizukami, S.; Takikawa, R.; Sugihara, F.; Hori, Y.; Tochio, H.; Waelchli, M.; Shirakawa, M.; Kikuchi, K. *J. Am. Chem. Soc.* **2008**, *130*, 794. (c) Cui, W.; Otten, P.; Li, Y.; Koeneman, K. S.; Yu, J.; Mason, R. P. *Magn. Reson. Med.* **2004**, *51*, 616. (d) Oishi, M.; Sumitani, S.; Nagasaki, Y. *Bioconjugate Chem.* **2007**, *18*, 1379.
(6) For recent reports on detecting the effects of reductases, see: (a) Robinson, S. P.; Griffiths, J. R. *Philos. Trans. R. Soc. London, Ser. B* **2004**, *359*, 987. (b) Krohn, K. A.; Link, J. M.; Mason, R. P. *Int. J. Nucl. Med.* **2008**, *49*, 129S. (c) Salmon, H. W.; Siemann, D. W. *Radiother. Oncol.* **2004**, *73*, 359.
(7) (a) Tanabe, K.; Hirata, N.; Harada, H.; Hiraoka, M.; Nishimoto, S. *ChemBioChem* **2008**, *9*, 426. (b) Zhang, Z.; Tanabe, K.; Hatta, H.; Nishimoto, S. *Org. Biomol. Chem.* **2005**, *3*, 1905.
(8) (a) Hernick, M.; Flader, C.; Borch, R. F. *J. Med. Chem.* **2002**, *45*, 3540. (b) Everett, S. A.; Swann, E.; Naylor, M. A.; Stratford, M. R. L.; Patel, K. B.; Tian, A.; Newman, R. G.; Vojnovic, B.; Moody, C. J.; Wardman, P. *Biochem. Pharmacol.* **2002**, *63*, 1629. (c) Swann, E.; Barraja, P.; Oberlander, A. M.; Gardipee, W. T.; Hundnott, A. R.; Beall, H. D.; Moody, C. J. *J. Med. Chem.* **2001**, *44*, 3311.
(9) (a) Kimura, A.; Narazaki, M.; Kanazawa, Y.; Fujiwara, H. *Magn. Reson. Imag.* **2004**, *22*, 855. (b) Kuribayashi, H.; Doi, Y.; Kanazawa, Y. *Magn. Reson. Med.* **2001**, *46*, 864.
(10) We observed slow reduction of IQ-F during the treatment with NQO1 that catalyzes two-electron reduction independent of the presence of oxygen. Therefore, IQ-F may not be an ideal substrate for NQO1. See Figure S6.
(11) Moore, W. J. *Physical Chemistry*; Prentice-Hall, Inc.: NJ, 1972.
(12) Yu, L. J.; Matis, J.; Scudiero, D. A.; Hite, K. M.; Monk, A.; Sausville, E. A.; Waxman, D. J. *Drug Metab. Dispos.* **2001**, *29*, 304.
(13) To prepare an aqueous solution of IQ-F, we employed a solubilization kit for hydrophobic drugs (PUREBRIGHT).
(14) McRobbie, D. W.; Moore, E. A.; Graves, M. J.; Prince, M. R. *MRI From Picture to Proton*; Cambridge University Press: Cambridge, 2003.
(15) An experimental detail was illustrated in Figure S4. See also Experimental Section described in the Supporting Information.

JA904953B